


Two-Dimensional Programmable Tweezer Arrays of Fermions

Zoe Z. Yan^{1,*}, Benjamin M. Spar^{1,*}, Max L. Prichard¹, Sungjae Chi¹, Hao-Tian Wei^{2,3},
 Eduardo Ibarra-García-Padilla^{2,3}, Kaden R. A. Hazzard^{2,3} and Waseem S. Bakr^{1,†}
¹*Department of Physics, Princeton University, Princeton, New Jersey 08544, USA*
²*Department of Physics and Astronomy, Rice University, Houston, Texas 77005, USA*
³*Rice Center for Quantum Materials, Rice University, Houston, Texas 77005, USA*

 (Received 28 March 2022; revised 27 June 2022; accepted 29 July 2022; published 14 September 2022)

We prepare high-filling two-component arrays of tens of fermionic ${}^6\text{Li}$ atoms in optical tweezers, with the atoms in the ground motional state of each tweezer. Using a stroboscopic technique, we configure the arrays in various two-dimensional geometries with negligible Floquet heating. A full spin- and density-resolved readout of individual sites allows us to postselect near-zero entropy initial states for fermionic quantum simulation. We prepare a correlated state in a two-by-two tunnel-coupled Hubbard plaquette, demonstrating all the building blocks for realizing a programmable fermionic quantum simulator.

DOI: [10.1103/PhysRevLett.129.123201](https://doi.org/10.1103/PhysRevLett.129.123201)

Ultracold atoms in optical tweezer arrays have become a popular platform for quantum simulation, computation, and metrology [1]. The tweezer platform has recently witnessed rapid breakthroughs, ranging from the development of precise optical clocks [2,3] to the demonstration of entangling operations [4–7]. The realization of defect-free arbitrary geometries [8,9], in particular in two dimensions, has paved the way for studying rich quantum many-body physics with localized Rydberg atoms, including frustrated spin models on a triangular lattice [10,11], topological phases in a zig-zag chain [12], and quantum spin liquids with atoms placed on the links of a kagome lattice [13].

The versatility of tweezer arrays has also been extended to systems of itinerant atoms where quantum statistics play a role [14–19]. In particular, tunnel-coupled arrays have been realized for small systems of bosonic [14] and fermionic [15–18] atoms in one-dimensional arrays. If these experiments can be scaled, they would constitute a bottom-up approach toward quantum simulation that complements optical lattice experiments with quantum gas microscopes, which currently lie at the forefront of studying one- and two-dimensional Hubbard models [20–29]. The difficulty of reconfiguring microscope experiments has led to an almost exclusive focus on physics in square lattices (Ref. [30] is a recent exception). Programmable Hubbard tweezer arrays would allow the extension of site-resolved studies to arbitrary lattice geometries that bring additional ingredients into play, including frustration, topology, and flat-band physics.

Hubbard tweezer arrays may also provide a route to address another major challenge for optical lattice experiments: the preparation of low-entropy phases of fermions. In optical lattice experiments, the entropy of the gas is limited by evaporative cooling, which is hindered by poor efficiencies at low temperatures. Entropy redistribution

schemes relying on the flow of entropy away from gapped phases have been proposed [31,32] and experimentally explored [33], but they have not resulted in significant reduction of achieved temperatures for correlated phases.

Here we show that stroboscopic optical tweezer arrays can be used to prepare fermionic systems with arbitrary two-dimensional (2D) geometry and entropies comparable to those achieved in optical lattices, with the additional advantage of being able to further reduce the entropy through postselection. This is possible due to several features particular to this platform. First, in loading a tweezer from a degenerate Fermi gas, the tweezer acts as a “dimple trap,” wherein the local Fermi temperature (T_F) is significantly higher than in the bulk gas. Since the fraction of atoms loaded into the tweezers is low, the temperature of the system remains approximately fixed to the bulk gas’s temperature, but the tweezers’ phase space density is enhanced. Furthermore, the occupancy of the lowest level of each tweezer (given by the Fermi-Dirac distribution) is close to unity. This enables the preparation of a state with two atoms in the ground motional state (one per spin state) on every tweezer with high fidelity, as first demonstrated in Ref. [34]. Second, the system can be evolved from the band insulator into a correlated state via an adiabatic ramp on of additional sites, taking advantage of independent tunability of each lattice site. We have previously shown that this technique can be used to prepare a state with antiferromagnetic correlations in an eight-site Fermi Hubbard chain [18]. We extend this approach to 2D and show that any preramp entropy in the system can be effectively eliminated by postselection on the atom number in each spin state. Postselection is enabled by spin- and density-resolved readout [22,35], which we implement in a bilayer imaging scheme.

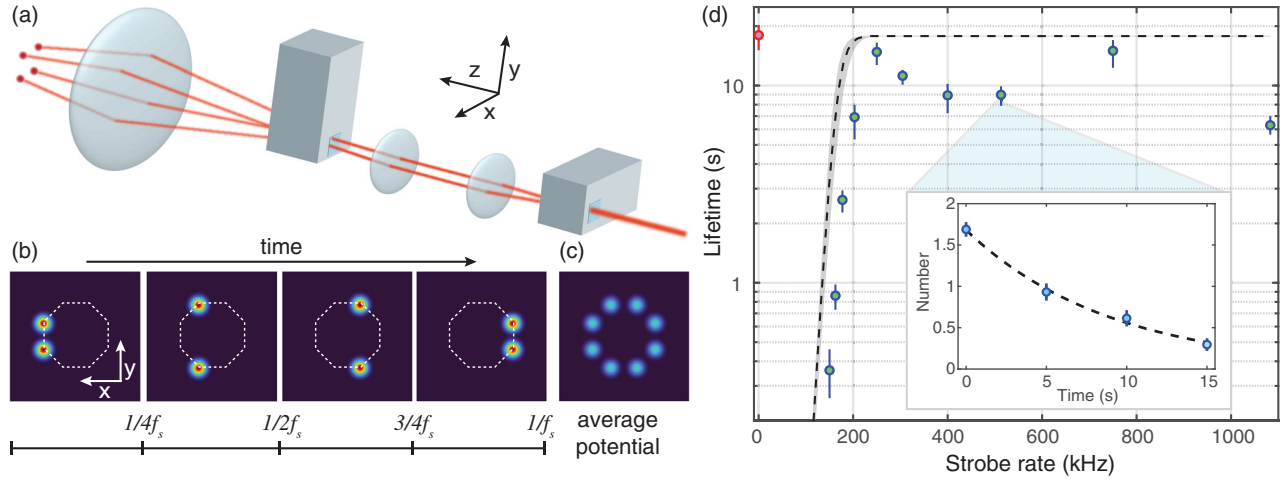


FIG. 1. 2D stroboscopic tweezer technique and lifetimes. (a) Two crossed acousto-optic modulators spaced in a $4f$ configuration generate the array. (b) Illustration of the principle of stroboscopic array generation of an eight-site ring. For a strobe frequency f_s , each column of the array is turned on for a quarter of the period $1/f_s$, generating a time-averaged potential shown in (c). (d) Lifetime of an atom in the ground vibrational state of a tweezer versus strobe frequency, with the red point at 0 kHz indicating the nonstrobed lifetime. The dashed line shows the theoretical prediction, and gray shading indicates the systematic uncertainties on the tweezer waist. The inset shows an example of a decay curve of population in the ground state for $f_s = 513$ kHz with an exponential fit.

The experimental cycle, including tweezer loading, is the same as detailed in Ref. [18]. Tweezers are loaded from a bulk Fermi gas at $T/T_F \approx 0.2$ that is a balanced mixture of the lowest and third lowest hyperfine ground states ($|\uparrow\rangle$, $|\downarrow\rangle$, respectively). Our scheme for generating 2D arrays uses two crossed acousto-optic modulators (AOMs) [Fig. 1(a)]. The tweezers are produced using light with a wavelength of 780 nm, and their waist at the atoms is 1000^{+180}_{-140} nm. Radiofrequency tones for both AOMs are generated by a two-channel arbitrary waveform generator, with a tone separation of 8 MHz corresponding to a tweezer spacing of 1350 nm in the atom plane. The aperture size and bandwidth of the modulators currently limit us to ~ 9 tweezers in each direction. The beat frequency of neighboring tweezers is > 100 times larger than typical tweezer depths, leading to negligible parametric heating.

Homogenizing the tweezer depths is particularly challenging for 2D arrays generated using crossed AOMs. A common approach used in Rydberg tweezer experiments is to apply a static set of frequencies consisting of n_x and n_y tones for the x - and y -directional AOMs, respectively. This generates a rectangular array of $n_x n_y$ sites; however, the $n_x + n_y$ degrees of freedom from the signal strength of each tone are insufficient to independently tune the depth of each tweezer. Better homogeneity can be achieved by tuning the relative phases of the tones, but the typical resultant inhomogeneity still exceeds 1%. Tunnel-coupled arrays have more stringent requirements for homogeneity, since the energy offsets in tweezers of a typical depth of $\sim h \times 50$ kHz must be controlled to within tunneling energies of $\sim h \times 250$ Hz, or better than 0.5%.

To homogenize arrays to within this precision and produce arrays with nearly arbitrary geometry (limited

by the optical resolution of our objective), we introduce a stroboscopic tweezer technique. We generate the array one column at a time, with different y -directional tones applied in every time step [Fig. 1(b)]. Effectively, the atoms experience a time-averaged potential of concatenated 1D arrays, as long as the strobe rate f_s far exceeds the tweezers' harmonic trap frequencies. As the typical axial (radial) trap frequencies are around 2.5 (15) kHz, we need strobe rates over an order of magnitude higher to avoid significant Floquet heating of the atoms.

We verify that the stroboscopic scheme is compatible with long lifetimes in the tweezer ground vibrational state with the following study. We measure the dependence of the lifetime in the lowest vibrational state on f_s in a two-site strobed array, varying the strobe rate from 163 to 1083 kHz, as shown in the Supplemental Material [36]. Higher frequencies are inaccessible due to limitations on the AOM response rate, set by the speed of sound and beam size in the crystal. We also compare the lifetimes to that of a static (nonstrobed) tweezer, which is limited by background gas collisions and off-resonant photon scattering due to the trapping light. Consistent with expectations, the lowest strobe rates give the shortest lifetimes in the ground state [Fig. 1(d)]. Measurements and numerics using a discrete variable representation method [36,44,45] both indicate that Floquet heating decreases exponentially with increasing f_s and is negligible for $f_s \gtrsim 250$ kHz, although the numerics underestimate the threshold frequency range below which severe heating occurs by $\sim 18\%$.

We demonstrate loading the arrays with band insulators of fermions with high fidelity using the stroboscopic method. These band insulators serve as low-entropy initial states for fermionic quantum simulation. As proofs of

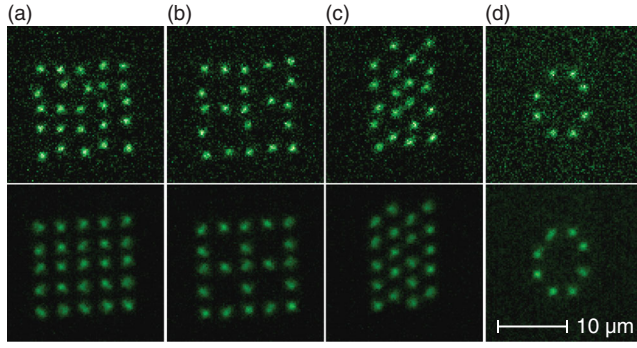


FIG. 2. Examples of band insulators of different geometries, showing (a) rectangular 5×5 , (b) 21-site Lieb plaquette, (c) 4×5 triangular, and (d) octagonal ring arrays. Only $|\uparrow\rangle$ atoms are imaged, and the sites here are not tunnel coupled. The top row shows single shots with perfect filling of the $|\uparrow\rangle$ state, and the bottom row shows average images. Deviations of the atom positions in the single-shot images are due to quantization onto the lattice for imaging. Average fillings of $|\uparrow\rangle$ are (93, 92, 91, 89)%, accounting for imaging fidelity of 98.5%, out of (411, 254, 275, 100) shots.

principle, we implement a rectangular 5×5 array, 21-site Lieb plaquette, triangular 4×5 array, and an eight-site octagonal ring (Fig. 2) [36]. The tweezers are homogenized using a density balancing algorithm where the number of required experimental shots is almost independent of the array size [18]. In these examples, the sites are not tunnel-coupled due to the large separations. Readout is accomplished by transferring the atoms into a 2D lattice of 752 nm spacing, which oversamples the tweezer array by a factor of 2 or more, and performing Raman sideband cooling on the $|\uparrow\rangle$ atoms after removal of the $|\downarrow\rangle$ atoms [18,23] with a detection fidelity of 98.5%. Throughout these different geometries, the loading fidelity of a single spin averages to 92%/site, corrected for imaging infidelity, indicating a low entropy of loading in the array. As in previous work [18,34], the tweezer depths are chosen so the predominant type of defect in each tweezer is a missing particle rather than an extra one in a higher motional state. In these data, we only measure one of the spin states in a given experimental shot, due to the problem of light-assisted collisions, which necessitates the removal of the other spin state before imaging [46].

To circumvent this problem and obtain full density resolution and spin resolution, we adopt a high-fidelity bilayer imaging scheme [35,47–49], which also allows the reduction of entropy upon postselection. A bilayer density readout and spin readout was first accomplished in fermionic quantum gas microscope experiments in a superlattice charge-pumping scheme [35]. Our method is conceptually similar but involves no superlattice (Fig. 3). Starting with tweezer-trapped atoms, we adiabatically turn off the tweezer and turn on a 2D lattice of 1064 nm and a vertical trap frequency of 1.2 kHz in 5 ms .

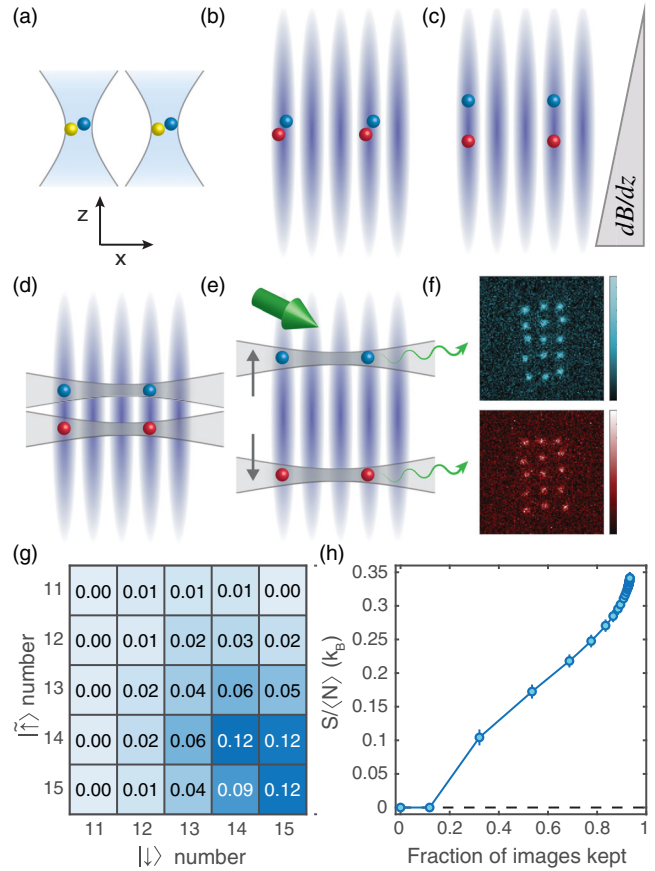


FIG. 3. Bilayer imaging procedure and entropy reduction through postselection. (a) Atoms in $|\uparrow\rangle$ (yellow) and $|\downarrow\rangle$ (blue) are initially trapped in the tweezers, then adiabatically loaded into (b) a 2D lattice with vertical waist of $75 \mu\text{m}$, where $|\uparrow\rangle$ is transferred to $|\tilde{\uparrow}\rangle$ (red). (c) A magnetic field gradient is applied to separate the spins in the vertical direction, after which (d) two lightsheet potentials turn on to fix the z positions. (e) The lightsheets are further separated to $25 \mu\text{m}$ separation. Raman sideband imaging commences, producing simultaneous images of both spin states. (f) Single-shot image of $|\downarrow\rangle$ and $|\tilde{\uparrow}\rangle$ originally from a 3×5 rectangular array. (g) Probability distribution versus number of atoms in each spin state over 972 shots. Here, all images with doublons (65 shots) were not used. (h) By postselecting on the maximum number of holes, effective entropy can be reduced by varying amounts.

The magnetic field is brought to 572 G , where we perform a spin flip of $|\uparrow\rangle$ to the second-lowest hyperfine state $|\tilde{\uparrow}\rangle$, with an efficiency exceeding 99%, and then decrease the field to near 0 G . Atoms in $|\tilde{\uparrow}\rangle$ and $|\downarrow\rangle$ have a greater differential magnetic moment than those in $|\uparrow\rangle$, enabling the Stern-Gerlach separation of these populations to $\sim 9 \mu\text{m}$ using a z -magnetic gradient of 168 G/cm in the 2D lattice at a depth of $280 E_R$. We turn on two lightsheet potentials [23]—highly anisotropic beams, each with z -directional trap frequencies of 26 kHz —and linearly ramp their vertical separation to $25 \mu\text{m}$ for imaging. We measure a combined transport and spin identification fidelity of

98.7%. Finally, we image the atoms using Raman sideband cooling simultaneously in both layers, with the 2D lattice depth at $2500 E_R$ and the two lightsheet z -trap frequencies at 70 kHz. Resulting fluorescence is collected by a high numerical aperture objective with atoms in the two planes focused onto two different active areas of a CCD camera. Imaging fidelity is 98% (97%) for the layer of $|\tilde{\uparrow}\rangle$ ($|\downarrow\rangle$) atoms.

Bilayer imaging enables reduction of the effective entropy associated with the initial state of the tweezer array (the band insulator) through postselection. The initial entropy per particle of the tweezer ensemble, assuming independent tweezers and single-band occupation, is given by

$$\frac{S}{\langle N \rangle} = -\frac{k_B}{p} (p \log p + (1-p) \log(1-p)). \quad (1)$$

where p is the probability to load one spin on a site. With a typical loading efficiency of $p = 0.907(3)$, the array starts with $0.34(1) k_B$ per particle, with entropy entering from microstates with undesired holes. By selecting only images with the population per spin state equal to the number of loading tweezers, we can effectively choose a subsample with $S = 0$. Importantly, this postselection criterion eliminates the initial state entropy even after changing the filling of the system (by introducing additional tweezers) to prepare a correlated state. The postselection criterion can be relaxed to use more images from the experiment at the cost of introducing additional initial state entropy. This trade-off is illustrated in Figs. 3(g)–3(h) for a 3×5 array in which $|\uparrow\rangle$ and $|\downarrow\rangle$ had average $p = 0.914(3)$ and $0.900(3)$, respectively (not accounting for imaging fidelity). Out of 972 images, 12% had perfect filling of 15 fermions of each species. However, even keeping images with up to two holes, or over 50% of shots, still results in a low entropy of $0.17(1) k_B$ per particle, which is favorable compared with state-of-the-art optical lattice experiments that range from 0.25 to $0.5 k_B$ per particle [25,33,50,51].

While postselection can be used to reduce the effective entropy of the initial state to near zero, subsequent ramps to correlated states will inevitably introduce additional entropy. Numerical simulations of the dynamical ramps in small systems indicate this extra entropy should be low for defect-free initial configurations. For example, for the ramp used in our previous work with an eight-site chain [18], the ramp is expected to have introduced an additional entropy of $0.04 k_B$ per particle when starting with a defect-free state, but the presence of even a single localized hole would lead to a significant entropy increase of 0.2 – $0.3 k_B$ per particle depending on the position of the hole. The entropy reported in Fig. 3(h) should therefore be treated only as a lower bound for future experiments.

Postselection on spin and density in this context should be distinguished from the context of optical lattice-based

quantum gas microscopy measurements. For example, in a recent study with a fermionic microscopes [51], spin readout and density readout enabled postselection of half filled systems with zero total magnetization, keeping $\sim 9\%$ of data. However, postselection there did not eliminate the finite spin temperature in the initial state. Furthermore, our postselection approach is difficult to implement in optical lattice systems where it has proven challenging to engineer arrays with sharp boundaries and a well-defined number of sites [33].

Equipped with the ability to load near-zero-entropy band insulators after postselection, we implement the simplest building block of a two-dimensional Fermi-Hubbard model: a tunnel-coupled 2×2 plaquette. The single-band Hamiltonian is

$$\begin{aligned} \hat{H} = & - \sum_{\langle i,j \rangle_{x,\sigma}} t_x (\hat{c}_{i\sigma}^\dagger \hat{c}_{j\sigma} + \text{H.c.}) - \sum_{\langle i,j \rangle_{y,\sigma}} t_y (\hat{c}_{i\sigma}^\dagger \hat{c}_{j\sigma} + \text{H.c.}) \\ & + \sum_i U_i \hat{n}_{i\uparrow} \hat{n}_{i\downarrow} + \sum_{i,\sigma} \Delta_i \hat{n}_{i\sigma}, \end{aligned} \quad (2)$$

where $\hat{c}_{i\sigma}^\dagger$ is the fermionic creation operator of spin σ at site i , $\hat{n}_{i\sigma}$ is the number operator, $t_{x(y)}$ is the tunneling matrix element in the $x(y)$ direction, Δ is the energy offset, and U is on site interaction between opposite spin states. We start by loading two diagonal sites in a rectangular array with vertical (horizontal) spacing of 1520 (1690) nm [Figs. 4(a) and 4(b)]. The correlated state at half filling is prepared by

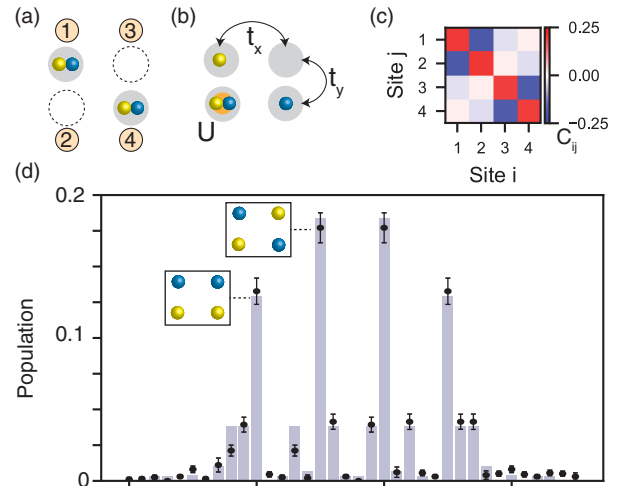


FIG. 4. Low entropy preparation of a 2×2 array. (a) We load two atoms per site on one diagonal of the array. (b) We create a correlated state by ramping on the additional lattice sites and increasing the scattering length to introduce on-site interactions. For the following data, we work with $t_x/h = 140(5)$ Hz, $t_y/h = 220(5)$ Hz, and $U/\bar{t} = 3.4(2)$. (c) Measured spin-spin correlations enabled by the bilayer imaging scheme. (d) Best fit (purple bars) and measured (black dots) microstate populations for 671 postselected experimental shots. The fit gives an entropy in the range $[0, 0.09] k_B$ per particle. Insets: the two most common states.

adiabatically ramping on the two opposing diagonal sites in 50 ms [18], with tunnelings of $t_x[t_y] = h \times 140(5)[220(5)]$ Hz in the final configuration [36]. We also ramp U/\bar{t} from 0 to 3.4(2) in the same time using the Feshbach resonance. Here, $\bar{t} = (t_x + t_y)/2$.

The resulting spin-spin correlations are shown in Fig. 4(c), which depicts $C_{ij} = \langle S_{z,i} S_{z,j} \rangle - \langle S_{z,i} \rangle \langle S_{z,j} \rangle$, where $S_{z,i} \equiv \frac{1}{2}(n_{\uparrow,i} - n_{\downarrow,i})$. Here, data were postselected to include only images that contained two $|\uparrow\rangle$ and two $|\downarrow\rangle$ atoms, for a total of 673 experimental cycles. With full spin readout and density readout, we are able to reconstruct the diagonals of the density matrix $\rho = |\Psi\rangle\langle\Psi|$ in the basis of allowed number states (with Hilbert space size $\binom{4}{2}^2 = 36$), and compare data with theory. In Fig. 4(d), we plot the experimental population in each microstate together with the populations expected theoretically for the plaquette ground state, which are consistent within error bars. Here, we reduce our statistical errors by taking advantage of the spin symmetry of the Hubbard Hamiltonian to average the probabilities for spin-reversed microstates. Furthermore, we fit the temperature of the canonical ensemble to best reproduce the distribution of microstates. The fit gives an upper bound for the temperature of $k_B T \sim 0.3\bar{t}$ (with the fit losing sensitivity below that temperature). This corresponds to an entropy in the range $[0, 0.09] k_B$ per particle, which is consistent with the prediction from simulating the ramp dynamics (entropy gain of $0.02 k_B$ per particle).

In conclusion, we have realized a 2D tweezer array of fermions with software-programmable geometry using a novel stroboscopic technique that allows independent control over all tweezer depths and positions. We have realized the building blocks to implement programmable 2D Fermi-Hubbard models, and demonstrated these on a small scale. Future work will focus on increasing the system size of the tunnel-coupled arrays. A natural target for future work will be few-leg ladder systems. For example, two-leg triangular ladder systems can be used to explore the J_1 - J_2 model, including the special case of the Majumdar-Ghosh model and its valence-bond solid ground states [52]. Furthermore, upon introducing spin imbalance and hole doping, a triangular two-leg ladder is predicted to host magnon-hole binding at energy scales set by the tunneling, rather than the superexchange [53]. Multileg triangular ladders may potentially host other exotic states such as a chiral spin liquid at half filling and intermediate U/t that evolves to a 120° -antiferromagnetic order at strong U/t [54]. Ultimately, fully 2D tunnel-coupled arrays with arbitrary geometry will be a rich playground for exploring novel phases of correlated fermions.

We would like to thank Grace Sommers and Elmer Guardado-Sanchez for experimental assistance and Martin Zwierlein's group for the loan of equipment. The experimental work was supported by the NSF (Grant No. 2110475), the David and Lucile Packard Foundation

(Grant No. 2016-65128), and the ONR (Grant No. N00014-21-1-2646). K. R. A. H., H.-T. W., and E. I.-G.-P. acknowledge support from the Welch Foundation through Grant No. C1872, the Office of Naval Research Grant No. N00014-20-1-2695, and the National Science Foundation through Grant No. PHY1848304. K. R. A. H. also benefited from discussions at the KITP, which was supported in part by the National Science Foundation under Grant No. NSF PHY-1748958.

*These authors contributed equally to this work.

†Corresponding author.

wbakr@princeton.edu

- [1] A. M. Kaufman and K.-K. Ni, *Nat. Phys.* **17**, 1324 (2021).
- [2] I. S. Madjarov, A. Cooper, A. L. Shaw, J. P. Covey, V. Schkolnik, T. H. Yoon, J. R. Williams, and M. Endres, *Phys. Rev. X* **9**, 041052 (2019).
- [3] A. W. Young, W. J. Eckner, W. R. Milner, D. Kedar, M. A. Norcia, E. Oelker, N. Schine, J. Ye, and A. M. Kaufman, *Nature (London)* **588**, 408 (2020).
- [4] T. M. Graham, M. Kwon, B. Grinkemeyer, Z. Marra, X. Jiang, M. T. Lichtman, Y. Sun, M. Ebert, and M. Saffman, *Phys. Rev. Lett.* **123**, 230501 (2019).
- [5] H. Levine, A. Keesling, G. Semeghini, A. Omran, T. T. Wang, S. Ebadi, H. Bernien, M. Greiner, V. Vuletić, H. Pichler, and M. D. Lukin, *Phys. Rev. Lett.* **123**, 170503 (2019).
- [6] A. Omran, H. Levine, A. Keesling, G. Semeghini, T. T. Wang, S. Ebadi, H. Bernien, A. S. Zibrov, H. Pichler, S. Choi *et al.*, *Science* **365**, 570 (2019).
- [7] I. S. Madjarov, J. P. Covey, A. L. Shaw, J. Choi, A. Kale, A. Cooper, H. Pichler, V. Schkolnik, J. R. Williams, and M. Endres, *Nat. Phys.* **16**, 857 (2020).
- [8] M. Endres, H. Bernien, A. Keesling, H. Levine, E. R. Anschuetz, A. Krajenbrink, C. Senko, V. Vuletic, M. Greiner, and M. D. Lukin, *Science* **354**, 1024 (2016).
- [9] D. Barredo, S. De Léséleuc, V. Lienhard, T. Lahaye, and A. Browaeys, *Science* **354**, 1021 (2016).
- [10] V. Lienhard, S. de Léséleuc, D. Barredo, T. Lahaye, A. Browaeys, M. Schuler, L.-P. Henry, and A. M. Läuchli, *Phys. Rev. X* **8**, 021070 (2018).
- [11] P. Scholl, M. Schuler, H. J. Williams, A. A. Eberharter, D. Barredo, K.-N. Schymik, V. Lienhard, L.-P. Henry, T. C. Lang, T. Lahaye *et al.*, *Nature (London)* **595**, 233 (2021).
- [12] S. de Léséleuc, V. Lienhard, P. Scholl, D. Barredo, S. Weber, N. Lang, H. P. Büchler, T. Lahaye, and A. Browaeys, *Science* **365**, 775 (2019).
- [13] G. Semeghini, H. Levine, A. Keesling, S. Ebadi, T. T. Wang, D. Bluvstein, R. Verresen, H. Pichler, M. Kalinowski, R. Samajdar *et al.*, *Science* **374**, 1242 (2021).
- [14] A. M. Kaufman, B. J. Lester, C. M. Reynolds, M. L. Wall, M. Foss-Feig, K. R. A. Hazzard, A. M. Rey, and C. A. Regal, *Science* **345**, 306 (2014).
- [15] S. Murmann, A. Bergschneider, V. M. Klinkhamer, G. Zürn, T. Lompe, and S. Jochim, *Phys. Rev. Lett.* **114**, 080402 (2015).

- [16] A. Bergschneider, V.M. Klinkhamer, J.H. Becher, R. Klemt, L. Palm, G. Zürn, S. Jochim, and P.M. Preiss, *Nat. Phys.* **15**, 640 (2019).
- [17] J.H. Becher, E. Sindici, R. Klemt, S. Jochim, A.J. Daley, and P.M. Preiss, *Phys. Rev. Lett.* **125**, 180402 (2020).
- [18] B.M. Spar, E. Guardado-Sanchez, S. Chi, Z.Z. Yan, and W.S. Bakr, *Phys. Rev. Lett.* **128**, 223202 (2022).
- [19] A.W. Young, W.J. Eckner, N. Schine, A.M. Childs, and A.M. Kaufman, [arXiv:2202.01204](https://arxiv.org/abs/2202.01204).
- [20] L.W. Cheuk, M.A. Nichols, K.R. Lawrence, M. Okan, H. Zhang, E. Khatami, N. Trivedi, T. Paiva, M. Rigol, and M.W. Zwierlein, *Science* **353**, 1260 (2016).
- [21] M.F. Parsons, A. Mazurenko, C.S. Chiu, G. Ji, D. Greif, and M. Greiner, *Science* **353**, 1253 (2016).
- [22] M. Boll, T.A. Hilker, G. Salomon, A. Omran, J. Nespolo, L. Pollet, I. Bloch, and C. Gross, *Science* **353**, 1257 (2016).
- [23] P.T. Brown, D. Mitra, E. Guardado-Sanchez, P. Schauß, S.S. Kondov, E. Khatami, T. Paiva, N. Trivedi, D.A. Huse, and W.S. Bakr, *Science* **357**, 1385 (2017).
- [24] M.A. Nichols, L.W. Cheuk, M. Okan, T.R. Hartke, E. Mendez, T. Senthil, E. Khatami, H. Zhang, and M.W. Zwierlein, *Science* **363**, 383 (2019).
- [25] P.T. Brown, D. Mitra, E. Guardado-Sanchez, R. Nourafkan, A. Reymbaut, C.-D. Hébert, S. Bergeron, A.-M. Tremblay, J. Kokalj, D.A. Huse *et al.*, *Science* **363**, 379 (2019).
- [26] J. Vijayan, P. Sompet, G. Salomon, J. Koepsell, S. Hirthe, A. Bohrdt, F. Grusdt, I. Bloch, and C. Gross, *Science* **367**, 186 (2020).
- [27] G. Ji, M. Xu, L.H. Kendrick, C.S. Chiu, J.C. Brüggenjürgen, D. Greif, A. Bohrdt, F. Grusdt, E. Demler, M. Lebrat, and M. Greiner, *Phys. Rev. X* **11**, 021022 (2021).
- [28] J. Koepsell, J. Vijayan, P. Sompet, F. Grusdt, T.A. Hilker, E. Demler, G. Salomon, I. Bloch, and C. Gross, *Nature (London)* **572**, 358 (2019).
- [29] A. Bohrdt, L. Homeier, C. Reinmoser, E. Demler, and F. Grusdt, *Ann. Phys. (Amsterdam)* **435**, 168651 (2021), special issue on Philip W. Anderson.
- [30] J. Yang, L. Liu, J. Mongkolkiattichai, and P. Schauss, *PRX Quantum* **2**, 020344 (2021).
- [31] J.-S. Bernier, C. Kollath, A. Georges, L. De Leo, F. Gerbier, C. Salomon, and M. Köhl, *Phys. Rev. A* **79**, 061601(R) (2009).
- [32] M. Lubasch, V. Murg, U. Schneider, J.I. Cirac, and M.-C. Bañuls, *Phys. Rev. Lett.* **107**, 165301 (2011).
- [33] C.S. Chiu, G. Ji, A. Mazurenko, D. Greif, and M. Greiner, *Phys. Rev. Lett.* **120**, 243201 (2018).
- [34] F. Serwane, G. Zürn, T. Lompe, T. Ottenstein, A. Wenz, and S. Jochim, *Science* **332**, 336 (2011).
- [35] J. Koepsell, S. Hirthe, D. Bourgund, P. Sompet, J. Vijayan, G. Salomon, C. Gross, and I. Bloch, *Phys. Rev. Lett.* **125**, 010403 (2020).
- [36] See Supplemental Material at <http://link.aps.org/supplemental/10.1103/PhysRevLett.129.123201> for the Floquet heating calculations and measurement techniques, details on the 2D array generation, and further discussion of the 2×2 plaquette data, which includes Refs. [37–43].
- [37] D. Neuhäuser and M. Baer, *J. Chem. Phys.* **90**, 4351 (1989).
- [38] J. Liang, R.N. Kohn Jr, M.F. Becker, and D.J. Heinzen, *Appl. Opt.* **48**, 1955 (2009).
- [39] N. Matsumoto, T. Inoue, T. Ando, Y. Takiguchi, Y. Ohtake, and H. Toyoda, *Opt. Lett.* **37**, 3135 (2012).
- [40] D. Kim, A. Keesling, A. Omran, H. Levine, H. Bernien, M. Greiner, M.D. Lukin, and D.R. Englund, *Opt. Lett.* **44**, 3178 (2019).
- [41] L. Bayha, M. Holten, R. Klemt, K. Subramanian, J. Bjerlin, S.M. Reimann, G.M. Bruun, P.M. Preiss, and S. Jochim, *Nature (London)* **587**, 583 (2020).
- [42] D. Mitra, P.T. Brown, P. Schauß, S.S. Kondov, and W.S. Bakr, *Phys. Rev. Lett.* **117**, 093601 (2016).
- [43] P. Weinberg and M. Bukov, *SciPost. Phys.* **7**, 020 (2019).
- [44] J.C. Light and T. Carrington Jr, *Adv. Chem. Phys.* **114**, 263 (2000).
- [45] M.L. Wall, K.R.A. Hazzard, and A.M. Rey, *Phys. Rev. A* **92**, 013610 (2015).
- [46] C. Gross and W.S. Bakr, *Nat. Phys.* **17**, 1316 (2021).
- [47] P.M. Preiss, R. Ma, M.E. Tai, J. Simon, and M. Greiner, *Phys. Rev. A* **91**, 041602(R) (2015).
- [48] T. Hartke, B. Oreg, N. Jia, and M. Zwierlein, *Phys. Rev. Lett.* **125**, 113601 (2020).
- [49] M. Gall, N. Wurz, J. Samland, C.F. Chan, and M. Köhl, *Nature (London)* **589**, 40 (2021).
- [50] A. Mazurenko, C.S. Chiu, G. Ji, M.F. Parsons, M. Kanász-Nagy, R. Schmidt, F. Grusdt, E. Demler, D. Greif, and M. Greiner, *Nature (London)* **545**, 462 (2017).
- [51] P. Sompet, S. Hirthe, D. Bourgund, T. Chalopin, J. Bibo, J. Koepsell, P. Bojović, R. Verresen, F. Pollmann, G. Salomon, C. Gross, T. Hilker, and I. Bloch, *Nature (London)* **606**, 484 (2022).
- [52] S.M. Girvin and K. Yang, *Modern Condensed Matter Physics* (Cambridge University Press, Cambridge, England, 2019).
- [53] I. Morera, A. Bohrdt, W.W. Ho, and E. Demler, [arXiv:2106.09600](https://arxiv.org/abs/2106.09600).
- [54] A. Szasz, J. Motruk, M.P. Zaletel, and J.E. Moore, *Phys. Rev. X* **10**, 021042 (2020).